Bull. Mater. Sci. (2021) 44:255
https://doi.org/10.1007/s12034-021-02543-x

Electrical properties of praseodymium and samarium co-doped ceria electrolyte for low-temperature solid oxide fuel cell application

LEMESSA ASEFA ERESSA[1,*] and P V BHASKARA RAO[2]
[1]Department of Physics, Ambo University, P.O. Box 19, Ambo, Ethiopia
[2]Department of Physics, Wollega University, P.O. Box 395, Nekemte, Ethiopia
*Author for correspondence (lemessaphys@gmail.com)

MS received 20 April 2021; accepted 12 July 2021

Abstract. In this study, we aimed to investigate the structural, morphology and electrical properties of praseodymium and samarium co-doped ceria electrolytes, synthesized using the sol–gel method, for use as an electrolyte in low-temperature solid oxide fuel cell (LT-SOFC) applications. The X-ray diffraction result shows that all of the samples crystallized into a single-phase cubic fluorite form. The average relative densities of samples sintered at 1400°C is 97.9% of theoretical densities, indicating that they can be used as an electrolyte in LT-SOFC applications. A fascinating and maximum value of ionic conductivity 1.94×10^{-2} S cm^{-1} and least activation energy (E_a = 0.55 eV) were found for the composition $Ce_{0.8}Sm_{0.1}Pr_{0.1}O_{1.9}$ at a temperature of 500°C. The ionic conductivity and activation energies of compositions $Ce_{0.85}Sm_{0.1}Pr_{0.05}O_{1.925}$ and $Ce_{0.9}Sm_{0.05}Pr_{0.05}O_{1.95}$ found at 500°C were (1.41×10^{-2} S cm^{-1}, E_a = 0.59 eV) and (5.95×10^{-3} S cm^{-1}, E_a = 0.64 eV), respectively. Moreover, all the Praseodymium and samarium co-doped ceria (PrSDC) samples conduct at lower temperature of 300°C. All these results confirmed that praseodymium and samarium co-doped ceria can be useful as a solid electrolyte in LT-SOFC applications.

Keywords. LT-SOFC; electrolyte; co-doping; electrical properties.

1. Introduction

Due to fascinating features, such as excellent performance, fuel flexibility and environmental friendliness, solid oxide fuel cells (SOFCs) are one of the most promising energy conversion devices [1–5]. However, SOFCs currently work at high temperatures (above 1000°C), which causes a number of issues, including thermal degradation of cell components, thermal expansion mismatch, prolonged start-up time, and unnecessary interfacial reaction between the electrodes and electrolyte, which in turn shorten the lifetime of the cell [6,7]. Furthermore, their high operating temperature range restricted their commercialization on a large scale [8,9].

As a result, it is preferable to produce electrolyte materials for SOFCs that can work at low temperatures (300 to 500°C) [10–12] for a variety of reasons, including improved efficiency and wide-scale commercialization [13]. In this regard, doped ceria electrolytes exhibit oxygen ionic conductivity and stability in SOFC applications at moderate and low temperatures [14–18]. However, there are challenges at lower temperatures, such as an increase in internal resistance of electric cell components for single-doped ceria with rare-earth elements, which is a critical factor for low ionic conductivity, resulting in poor cell efficiency [19–21]. A low ionic conductivity was reported for single-doped ceria with praseodymium (1.213×10^{-3} S cm^{-1} at 700°C) [22] and samarium (1.7×10^{-3} S cm^{-1} at 500°C) [23] due to the aforementioned factors. Co-doping method is a better approach in order to solve all these challenges [17,24–27] with selective rare-earth elements. As a result, this research aimed to investigate the structural and electrical properties of $Ce_{1-x-y}Sm_x Pr_y O_{2-\delta} (x = y = 0.05, x = y = 0.1, x = 0.1$ and $y = 0.05)$ materials synthesized using the sol–gel method for use as an electrolyte in LT-SOFC applications.

2. Experimental

Commercially available cerium nitrate hexahydrate ($(Ce(NO_3)_3{\cdot}6H_2O$; 99.99% purity)), samarium nitrate hexahydrate ($(Sm(NO_3)_3{\cdot}6H_2O$); 99.99% purity) praseodymium (III) nitrate hexahydrate ($(Pr(NO_3)_3{\cdot}6H_2O$); 99.99% purity), ammonium hydroxide (NH_4OH), citric acid ($C_6H_8O_7$) and ethylene glycol ($CH_3COOC_2H_5$) were used as starting chemicals for the preparation of PrSDC samples using sol–gel method. The first step was dissolving stoichiometric quantities of all nitrates in distilled water while continuously stirring. To retain the overall molar ratio of metal to citric acid, citric acid was added to the entire

Published online: 23 September 2021

mixture of precursors in a 1:1 molar ratio. Ammonium hydroxide was applied to the solution drop by drop to bring the pH to 7. The entire mixture was then stirred for 3 h at 80°C to form a homogeneous solution. After 3 h, a viscous gel was formed, which was then baked into an ash. To extract the carbonaceous compounds, the ash was calcined at 700°C for 2 h. To make a fine homogeneous powder, the resulting ash was ground continuously for 1 h in an agate mortar. To make a fine homogeneous powder, the resulting ash was ground continuously for 1 h in an agate mortar. The powders were pressed into a circular pellet using a hydraulic press at a pressure of 200 MPa (8 mm in diameter and 2 mm in thickness). Finally, the pellets were sintered for 2 h at 1400°C in a furnace before being prepared for other measurements.

3. Results and discussions

3.1 *X-ray diffraction analysis*

The X-ray diffraction (XRD) patterns obtained from all PrSDC samples prepared by sintering at 1400°C for 2 h are shown in figure 1. All of the peaks represent the normal fluorite structure of ceria (111, 200, 220, 311, 222, 400, 331, 420 and 422), which are consistent with the JCPDS 34-0394 standard's characteristic diffraction pattern of face-centred cubic structure of CeO_2 (space group Fm3m) [28–31]. No diffraction peaks resulting from impurity phases were observed in all PrSDC samples, suggesting the formation of a homogeneous single polycrystalline phase. The diffraction pattern also indicates that the crystallites are in nano scale with size of 14 nm.

The experimental lattice parameters of $Ce_{0.9}Sm_{0.05}Pr_{0.05}O_{1.95}$, $Ce_{0.85}Sm_{0.1}Pr_{0.05}O_{1.925}$ and $Ce_{0.8}Sm_{0.1}Pr_{0.1}O_{1.9}$ were 5.422, 5.426 and 5.423 Å, respectively, and are depicted in table 1. These values are slightly larger than lattice parameter of pure CeO_2 (5.411 Å) [32], as expected from the substitution of Ce^{4+} with larger effective ionic radii of Pr^{3+} and Sm^{3+} [33]. This also demonstrates that the PrSDC samples' lattice parameters differ from those of pure CeO_2, indicating that all the dopants were dissolved in the solution forming a homogenous solid material.

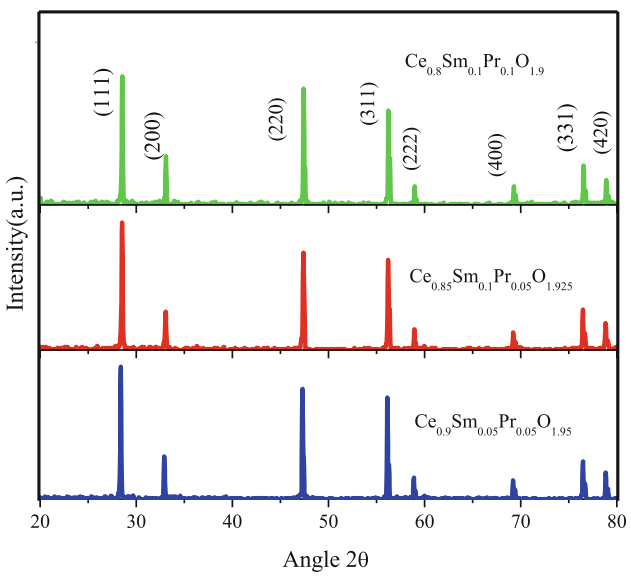

Figure 1. XRD patterns of PrSDC samples.

3.2 *SEM and EDX analysis*

Figures 2 and 3 depict the surface morphology and chemical compositions of PrSDC samples, as observed and analysed by scanning electron microscopy (SEM) and energy dispersive X-ray (EDX), respectively. The presence of faceted grains is clearly visible in the SEM micrograph. Table 1 shows the average grain sizes 451.4, 350 and 418.2 nm for compositions $Ce_{0.9}Sm_{0.05}Pr_{0.05}O_{1.95}$, $Ce_{0.85}Sm_{0.1}Pr_{0.05}O_{1.925}$ and $Ce_{0.8}Sm_{0.1}Pr_{0.1}O_{1.9}$, respectively. The difference of grain size observed among samples is a result of ionic radius variation between the co-dopants samarium and praseodymium and their concentrations. Moreover, it is created due to their morphology differences, which resulted with non-uniform treatments during the synthesis of samples. These values are within the range of grain sizes, previously stated for Pr-doped ceria in the literature [31,34].

To assess the degree of porosity in prepared samples, density measurements were taken. Using Archimedes' theory and xylene as a fluid, the experimental densities of PrSDC samples were determined. The relative density (η) is measured as a ratio of the sample experimental density (D_e) to the theoretical density [33] expressed in percentages:

$$\eta = \frac{D_e}{D_t} \times 100\% \quad (1)$$

The calculated relative densities of these samples were approximately 97.9% of the theoretical densities, as shown in table 1, and these results were confirmed by SEM images depicted in figure 2. The high densification (negligible porosity) of PrSDC samples discovered in this study has an important impact on their ionic conductivities. These findings were also supported by SEM images. The EDX graph in figure 3 verified the existence of elements Pr, Sm, Ce and O in the PrSDC samples, with no other elements detected. Furthermore, the atomic weights of the elements Pr, Sm, Ce and O present in each sample were calculated using stoichiometry, and their atomic percentages are listed in table 2.

3.3 *Raman spectroscopy analysis*

The Raman spectra of the PrSDC samples (shown in figure 4) reveal the existence of two distinct peaks. The F_{2g} vibration mode of pure CeO_2 is responsible for the peak at lower wavenumber (456–463) cm^{-1}. Furthermore, the peak

Table 1. Grain size, experimental lattice parameter and relative densities of PrSDC samples.

Compositions	Crystallite Size (nm)	Grain size (nm)	Lattice parameter (Å)	Theoretical density (g cm^{-3})	Experimental density (g cm^{-3})	Relative density
$Ce_{0.9}Sm_{0.05}Pr_{0.05}O_{1.95}$	14	451.4	5.422	7.22186	7.12768	98.7
$Ce_{0.85}Sm_{0.1}Pr_{0.05}O_{1.925}$	14	350	5.426	7.22648	7.14671	98.9
$Ce_{0.8}Sm_{0.1}Pr_{0.1}O_{1.9}$	14	418.2	5.423	7.21142	7.05857	97.9

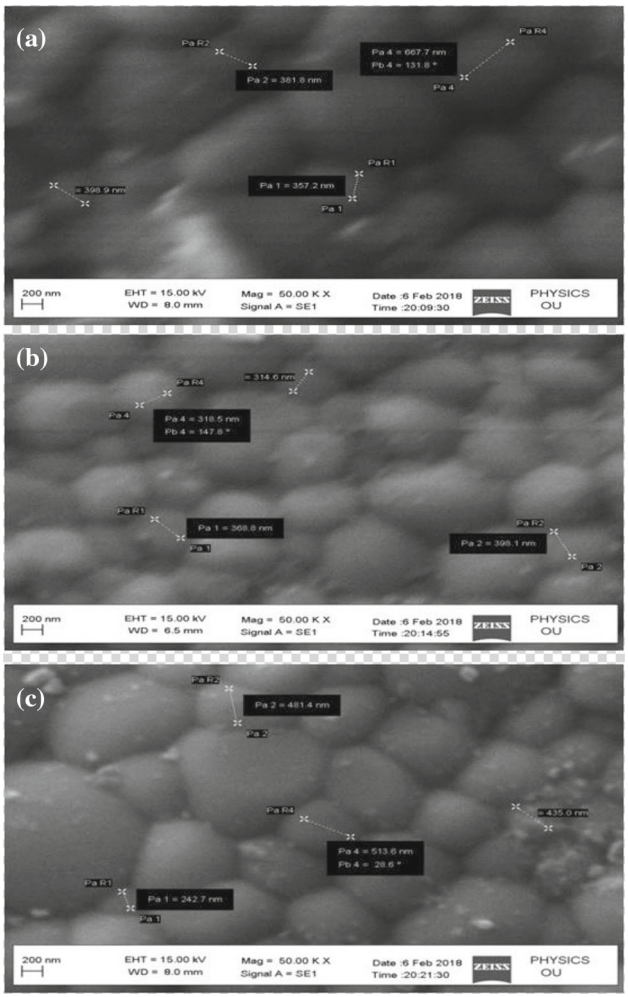

Figure 2. SEM graphs of (**a**) $Ce_{0.9}Sm_{0.05}Pr_{0.05}O_{1.95}$, (**b**) $Ce_{0.85}Sm_{0.1}Pr_{0.05}O_{1.925}$ and (**c**) $Ce_{0.8}Sm_{0.1}Pr_{0.1}O_{1.9}$.

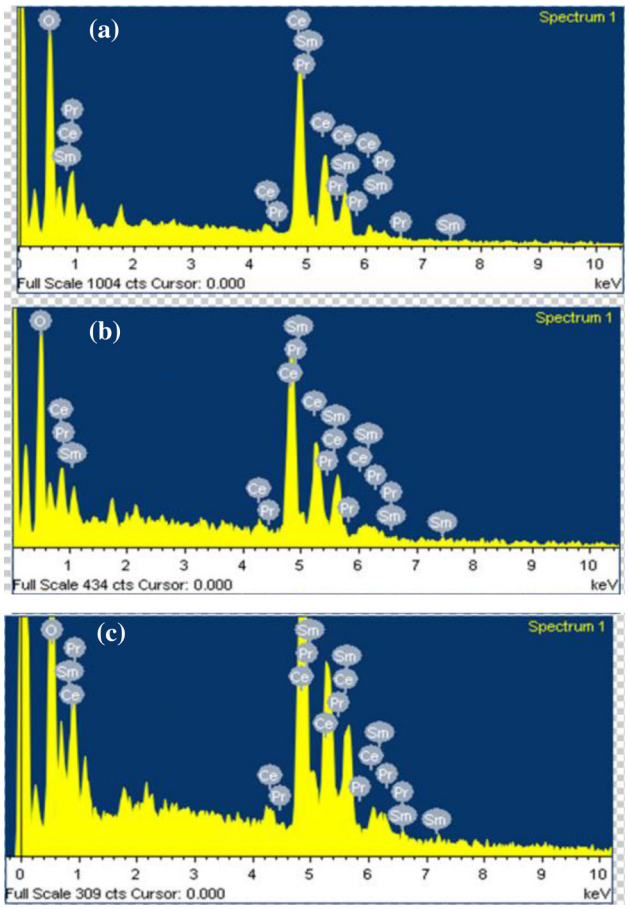

Figure 3. EDX graphs of (**a**) $Ce_{0.9}Sm_{0.05}Pr_{0.05}O_{1.95}$, (**b**) $Ce_{0.85}Sm_{0.1}Pr_{0.05}O_{1.925}$ and (**c**) $Ce_{0.8}Sm_{0.1}Pr_{0.1}O_{1.9}$.

at higher wavenumber (564–572) cm^{-1} can be attributed to oxygen vacancies inserted extrinsically into PrSDC samples for charge neutrality maintenance. The changes in the Raman spectra are related to oxygen (O) vacancies produced in the cation lattice (Pr^{3+} and Sm^{3+}) substituted for Ce^{4+}. Furthermore, since none of these samples indicated a characteristic vibration mode at 360 cm^{-1}, which would arise from a Pr_2O_3 and Sm_2O_3 cubic phase, it can be concluded that Pr_2O_3 and Sm_2O_3 have fully dissolved into the fluorite structure of ceria. This pattern of results was previously observed in the literature for Pr-doped ceria electrolytes [31,35–37]. As the concentration of Pr increases, the F_{2g} band shifts to a lower wavenumber, which is followed by a decrease in peak intensity. This is due to Pr^{3+} (1.126 Å) and Sm^{3+} (1.08 Å) having greater ionic radius than Ce^{4+} (0.97 Å), which contradicts the XRD analysis, and shows an increase in the lattice parameter with increase in Pr atom.

In comparison, as the Pr concentration in the PrSDC samples increases, the second peak in the Raman spectra at about 564–572 cm^{-1} rises dramatically. Because of the impact of doping with Pr^{3+} or Sm^{3+} on CeO_2, the PrSDC samples will have a higher oxygen vacancy concentration.

Table 2. EDX quantitative analysis of elements O, Ce, Sm and Pr.

Co-doped ceria	Weight (%)				Atomic (%)			
	O K	Ce L	Pr L	Sm L	O K	Ce L	Pr L	Sm L
$Ce_{0.9}Sm_{0.05}Pr_{0.05}O_{1.95}$	19.26	67.90	6.38	6.46	67.76	27.87	2.25	2.12
$Ce_{0.85}Sm_{0.1}Pr_{0.05}O_{1.925}$	18.15	66.78	4.74	10.33	66.21	27.82	1.96	4.01
$Ce_{0.8}Sm_{0.1}Pr_{0.1}O_{1.9}$	18.33	63.86	9.14	8.66	66.46	26.44	3.76	3.34

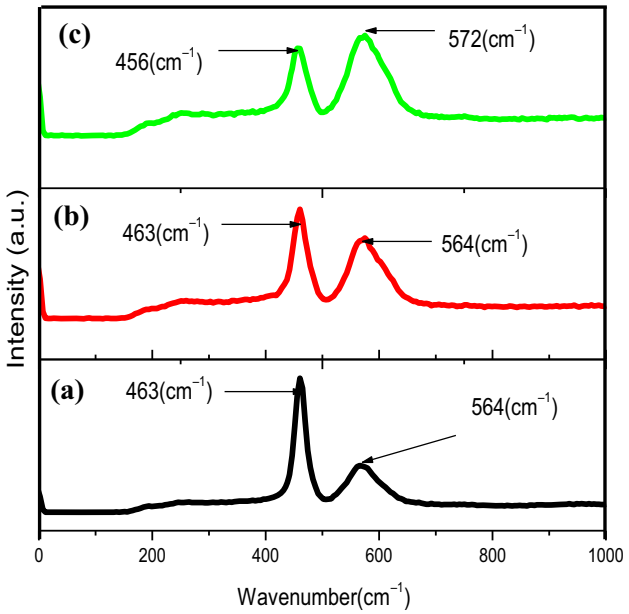

Figure 4. Raman spectra of (a) $Ce_{0.9}Sm_{0.05}Pr_{0.05}O_{1.95}$, (b) $Ce_{0.85}Sm_{0.1}Pr_{0.05}O_{1.925}$ and (c) $Ce_{0.8}Sm_{0.1}Pr_{0.1}O_{1.9}$.

As a result, the increased oxygen vacancy concentration in Pr and Sm co-doped cerium oxide is indicated by the monotonic increase of 564–572 cm^{-1} peak intensity with respect to Pr or Sm content, as in figure 4. Finally, when comparing PrSDC samples, the Raman peak at 564–572 cm^{-1} for $Ce_{0.8}Sm_{0.1}Pr_{0.1}O_{1.9}$ composition is the highest compared to other samples. This is because this sample has the largest concentration of oxygen vacancies compared to others. No indications of impurities can be found in the Raman spectroscopy analysis, which is in good agreement with the XRD analysis depicted in figure 1.

3.4 *Impedance spectroscopy*

AC impedance measurements were taken in air at temperatures ranging from 300 to 500°C. Figure 5a–d shows impedance plots of PrSDC samples as a function of Pr and Sm content calculated at different temperatures. The typical impedance spectra show semi-depressed arcs at medium frequency and incomplete arc at low frequency range. However, due to the limited frequency of measuring equipment, the arc in the high frequency range is not displayed (1 Hz–1 MHz). The grain resistance is defined as the length of a real axis, for which the arc is not displayed.

As a result, the grain resistance (R_g) was represented by the left horizontal axis, while R_{gb} was calculated by fitting the medium frequency arc intercept to the real axis. In previous literatures, this impedance behaviour was also described for doped ceria [38–42]. The total resistance is given by

$$R = R_g + R_{gb}, \tag{2}$$

where R_g and R_{gb} stand for the resistance of grain interior and grain boundary, respectively. Then, the ionic conductivity (σ) of each sample was calculated using the equation:

$$\sigma = \frac{l}{RA}, \tag{3}$$

where l is the thickness of sample and A the cross-sectional area. Through curve fitting a circle to the semicircles in figure 5a–d, and values of grain and grain boundary resistance values were determined and depicted in tables 3, 4 and 5.

The grain resistance (R_g) increased slowly, but the grain boundary resistance (R_{gb}) decreased dramatically as the Pr concentration increased from 5 to 10 mol% with temperature, as shown in tables 3, 4 and 5. This means that increase in the amount of Pr has a small impact on grain resistance, but a big impact on grain boundary resistance.

Throughout the temperature spectrum, the $Ce_{0.8}Sm_{0.1}Pr_{0.1}O_{1.9}$ composition has the highest conductivity, while the $Ce_{0.9}Sm_{0.05}Pr_{0.05}O_{1.95}$ composition has the lowest. Taking the ratio of their conductivities, $Ce_{0.8}Sm_{0.1}Pr_{0.1}O_{1.9}$ has a conductivity of 1.37 times that of $Ce_{0.85}Sm_{0.1}Pr_{0.05}O_{1.925}$ and 3.26 times that of $Ce_{0.9}Sm_{0.05}Pr_{0.05}O_{1.95}$ at 500°C air temperature, as shown in tables 3, 4 and 5. This is basically due to the formation of more oxygen vacancies and fast diffusion of these charge carriers at triple phase boundary in $Ce_{0.8}Sm_{0.1}Pr_{0.1}O_{1.9}$ sample than $Ce_{0.85}Sm_{0.1}Pr_{0.05}O_{1.925}$ or $Ce_{0.9}Sm_{0.05}Pr_{0.05}O_{1.95}$. This is supported with the highest Raman second peak (564–572 cm^{-1}) of $Ce_{0.8}Sm_{0.1}Pr_{0.1}O_{1.9}$ than both samples, as shown in figure 4.

The temperature dependence of ionic conductivity often follows an Arrhenius relation:

$$\sigma T = \sigma_o e^{-Ea/kT}, \tag{4}$$

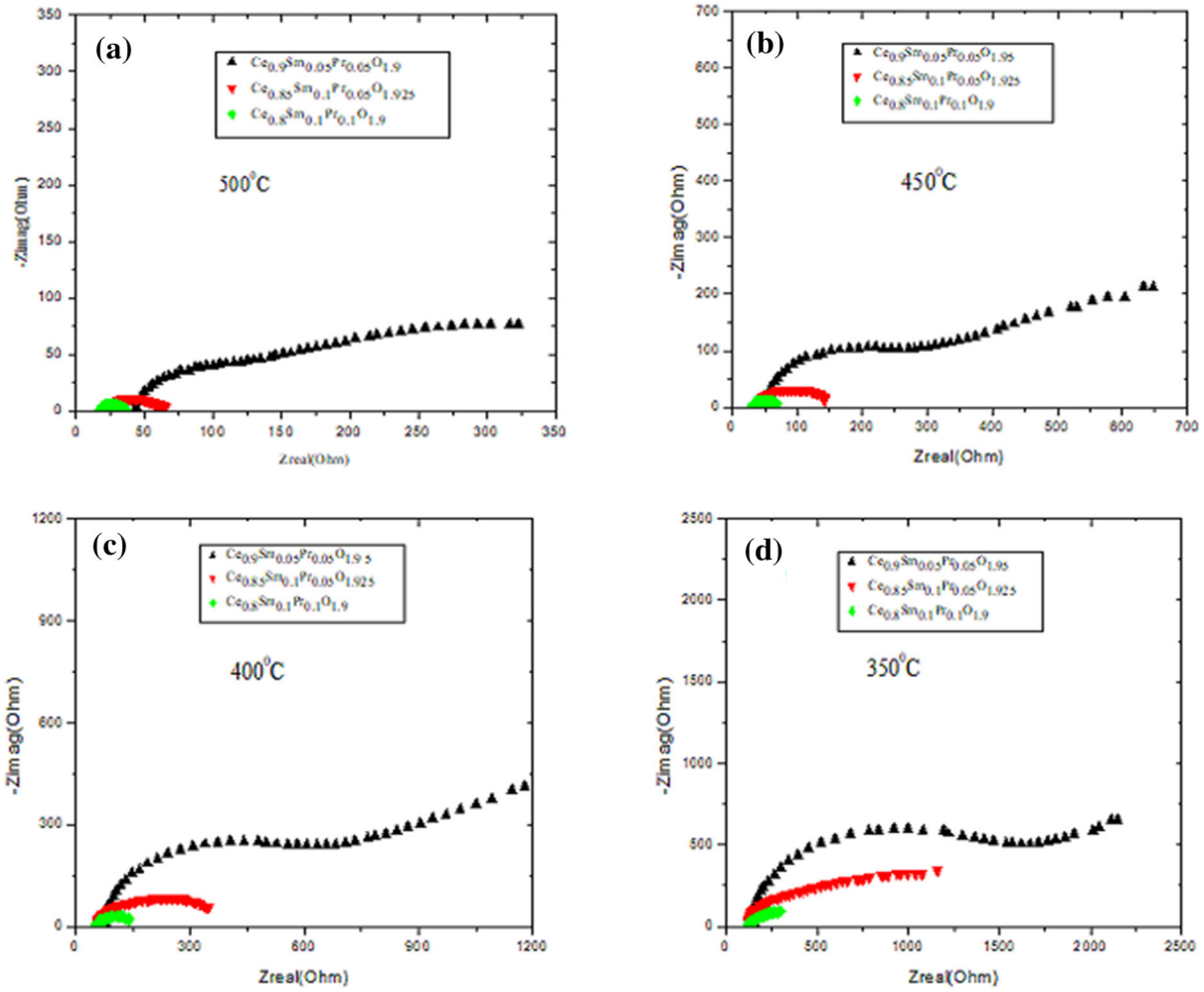

Figure 5. Impedance plots of PrSDC samples at (**a**) 500, (**b**) 450, (**c**) 400 and (**d**) 350°C.

Table 3. Resistances and conductivities of $Ce_{0.9}Sm_{0.05}Pr_{0.05}O_{1.95}$ sample.

Temperature (°C)	$R_g(\Omega)$	$R_{gb}(\Omega)$	$R_T(\Omega)$	σ (S cm^{-1})
300	260.85	2225.75	2486.16	2.87×10^{-4}
350	146.53	931.9	1078.43	6.62×10^{-4}
400	78.54	361.87	440.41	1.62×10^{-3}
450	52.4	168.38	220.8	3.23×10^{-3}
500	44.27	75.73	120.0	5.95×10^{-3}

Table 4. Resistances and conductivities of $Ce_{0.85}Sm_{0.1}Pr_{0.05}O_{1.925}$ sample.

Temperature (°C)	$R_g(\Omega)$	$R_{gb}(\Omega)$	$R_T(\Omega)$	σ (S cm^{-1})
300	207.41	616.55	823.96	8.67×10^{-4}
350	131.09	265.22	396.31	1.8×10^{-3}
400	56.44	129.47	185.91	3.84×10^{-3}
450	36.65	58.76	95.41	7.48×10^{-3}
500	23.13	27.46	50.59	1.41×10^{-2}

where E_a is the activation energy for conduction, T the temperature, k the Boltzmann's constant and σ_o is a pre-exponential factor. The total ionic conductivities of PrSDC samples are presented (figure 6) in the form of $\ln(\sigma T)$ *vs.* (10^3/T). The value of E_a was found from the slope of the graph.

Figure 6 shows Arrhenius plots for PrSDC samples. With increase in temperature, the conductivity of PrSDC samples increases exponentially. This could be due to thermal

Table 5. Resistances and conductivities of $Ce_{0.8}Sm_{0.1}Pr_{0.1}O_{1.9}$ sample.

Temperature (°C)	$R_g(\Omega)$	$R_{gb}(\Omega)$	$R_T(\Omega)$	σ (S cm^{-1})
300	225.39	239.3	464.69	1.53×10^{-3}
350	117.16	127.75	244.91	2.91×10^{-3}
400	53.87	68.72	122.42	5.83×10^{-3}
450	32.26	35.29	67.55	1.05×10^{-2}
500	17.7	19.11	36.81	1.94×10^{-2}

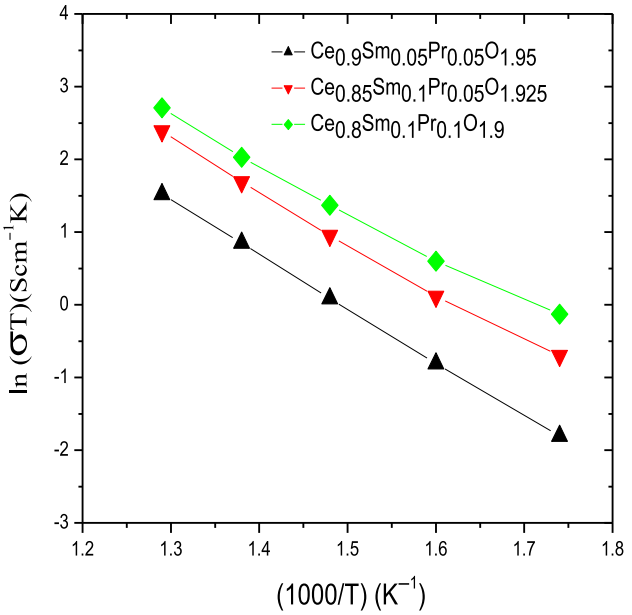

Figure 6. Arrhenius plots for total conductivity of PrSDC samples.

Table 6. Activation energy of PrSDC samples.

Samples	E_a (eV)
$Ce_{0.9}Sm_{0.05}Pr_{0.05}O_{1.95}$	0.64
$Ce_{0.85}Sm_{0.1}$ $Pr_{0.05}O_{1.925}$	0.59
$Ce_{0.8}Sm_{0.1}$ $Pr_{0.1}O_{1.9}$	0.55

excitation, which boosts carrier kinetic energy and forces oxygen ions to pass through oxygen vacancies faster. As the temperature increases, oxygen ions have a greater tendency to diffuse, resulting in increased conductivity.

As shown in figure 6, the graph of $Ce_{0.8}Sm_{0.1}Pr_{0.1}O_{1.9}$ is higher than the graphs of the other PrSDC samples. This indicates that this sample has the highest conductivity of all the PrSDC samples. This may be attributed to the creation of more oxygen vacancies in $Ce_{0.8}Sm_{0.1}Pr_{0.1}O_{1.9}$ than in other PrSDC samples. The activation energy for diffusion of O^{2-} ions in $Ce_{0.8}Sm_{0.1}Pr_{0.1}O_{1.9}$ sample decreases as a result of this phenomenon [43].

The activation energy of PrSDC samples obtained by fitting the data, in figure 6, to Arrhenius relations (equation 4) is shown in table 6. The value of this activation energy decreases as the concentration of Pr and Sm dopants increases.

This may be attributed to increased oxygen vacancy output and oxygen ion diffusion as the amount of dopants increases. This result is consistent with previous findings for single Pr-doped ceria electrolytes in the literature [44]. Because of the above reasons, the observed ionic conductivity of all PrSDC samples was greater than that of single Pr-doped ceria in this study.

The average radius of dopant ions tends to be similar to the critical ionic radius (r_c = 1.038 Å) when the smaller Ce^{4+} (0.97 Å) is replaced by a mixture of Pr^{3+} (1.126 Å) and Sm^{3+} (1.07 Å), which can minimize lattice distortion and facilitate oxygen ion diffusion in the lattice. As shown in the Raman spectra, Pr and Sm dopants increased the concentration of oxygen vacancies, which is beneficial to the migration of oxygen ions through oxygen vacancies. Because of these factors, the conductivity of Pr and Sm co-doped ceria improved over that of single Pr-doped ceria.

4. Conclusion

Praseodymium and samarium co-doped ceria samples were successfully prepared through sol–gel method. According to the XRD results, the entire PrSDC sample is a single phase with a cubic fluorite-like structure. The average grain size of particles found from SEM picture was in the range of 350–451nm. According to AC impedance analysis, the conductivity increased monotonically as the amount of praseodymium and samarium in the sample increased. The composition $Ce_{0.8}Sm_{0.1}Pr_{0.1}O_{1.9}$ showed the highest ionic conductivity (1.94×10^{-2} S cm^{-1}) and least activation energy (E_a = 0.55 eV) in the series of PrSDC samples at 500°C in air atmosphere. $Ce_{0.8}Sm_{0.1}Pr_{0.1}O_{1.9}$ has a higher conductivity than $Ce_{0.9}Sm_{0.05}Pr_{0.05}O_{1.95}$ when the ratio of Sm and Pr is 1:1. The ionic conductivity value obtained in our study at such a low operating temperature, 500°C, was found to be higher than previously recorded values for single-doped ceria with praseodymium. Furthermore, all experimental findings showed that the material prepared from praseodymium and samarium co-doped ceria can be used as an electrolyte for LT-SOFC applications.

References

[1] Singhal S C and Kendall K 2003 *High-temperature solid oxide fuel cells: Fundamentals, design and applications Elsevier Science* **1** 83
[2] Mat M D, Liu X, Zhu Z and Zhu B 2007 *Int. J. Hydrogen Energy* **32** 796
[3] Park S, Vohs J M and Gorte R J 2000 *Nature* **404** 265
[4] Choudhury A, Chandra H and Arora A 2013 *Ren. Sust. Energy Rev.* **20** 430
[5] Wang F-Y, Chen S, Wang Q, Yu S and Cheng S 2004 *Catal. Today* **97** 189
[6] Mizutani Y, Tamura M, Kawai M and Yamamoto O 1994 *Solid State Ion.* **72** 271
[7] Taroco H A, Santos J A F, Domingues R Z and Matencio T 2011 *Adv. Ceram Brasil* **307** 423
[8] Brant M, Matencio T, Dessemond L and Domingues R 2006 *Solid State Ion.* **177** 915
[9] Jaiswal N, Tanwar K, Suman R, Kumar D, Upadhyay S and Parkash O 2019 *J. Alloys Comp.* **781** 984

[10] Gao Z, Mogni L V, Miller E C, Railsback J G and Barnett S A 2014 *Energy Environ. Sci* **9** 1602
[11] Wachsman E D and Lee K T 2011 *Science* **334** 935
[12] Zha S, Xia C and Meng G 2003 *J. Power Sources* **115** 44
[13] Arabacı A and Öksüzömer M F 2012 *Ceram. Int.* **38** 6509
[14] Altaf F, Batool R, Gill R, Abbas G, Raza R, Khan M A *et al* 2019 *Ceram. Int.* **45** 10330
[15] Suzuki T, Funahashi Y, Yamaguchi T, Fujishiro Y and Awano M 2009 *Electrochem.* **77** 134
[16] Maricle D, Swarr T and Karavolis S 1992 *Solid State Ion.* **52** 173
[17] Raharjo J, Setya Aninda R and Ami Lestari N 2017 *J. Phys. Conf. Series* **123** 012077
[18] Aydin F, Demir I and Mat M 2014 *Int. J. Eng. Sci. Technol.* **17** 25
[19] Liu M, Uba F and Liu Y 2020 *J. Am. Ceram. Soc.* **103** 5325
[20] Fan L, Zhu B, Su P-C and He C 2018 *Nano Energy* **45** 148
[21] Eressa L A and Rao P B 2020 *Mater. Chem. Phys.* **242** 121914
[22] Irfana S, Junsung A, Parvathi N, Srikar M, Sunaina P, Nivedithaa V *et al* 2018 *Mater. Chem. Phys.* **05** 136
[23] Bhabu K A, Theerthagiri J, Madhavan J, Balu T, Muralidharan G and Rajasekaran T R 2016 *J. Mater. Sci.: Mater. Electron.* **27** 1566
[24] Preethi S and Babu K S 2012 *J. Alloys Comp.* **792** 1068
[25] Singh N, Singh N K, Kumar D and Parkash O 2012 *J. Alloys Comp.* **519** 129
[26] Jaiswal N, Kumar D, Upadhyay S and Parkash O 2014 *Ionics* **20** 45
[27] Puente-Martínez D, Díaz-Guillén J, Montemayor S, Díaz-Guillén J, Burciaga-Díaz O, Bazaldúa-Medellín M *et al* 2020 *Int. J. Hydrogen Energy* **45** 14062
[28] Swatsitang E, Phokha S, Hunpratub S and Maensiri S 2016 *Mater. Des.* **108** 27
[29] Piumetti M, Bensaid S, Andana T, Dosa M, Novara C, Giorgis F *et al* 2017 *Catalysts* **7** 174
[30] Spanier J E, Robinson R D, Zhang F, Chan S-W and Herman I P 2001 *Phys. Rev. B* **64** 245407
[31] Eressa L A and Rao P B 2020 *Chem. Tech.* **12** 28
[32] Dos Santos M, Lima R, Riccardi C, Tranquilin R, Bueno P R, Varela J A *et al* 2008 *Mater. Lett.* **62** 4509
[33] Stojmenović M, Žunić M, Gulicovski J, Bajuk-Bogdanović D, Holclajtner-Antunović I, Dodevski V *et al* 2015 *J. Mater. Sci.* **50** 3781
[34] Jeyanthi C E, Siddheswaran R, Kumar P, Chinnu M K, Rajarajan K and Jayavel R 2015 *Mater. Chem. Phys.* **151** 22
[35] Shajahan I, Ahn J, Nair P, Medisetti S, Patil S, Niveditha V *et al* 2018 *Mater. Chem. Phys.* **216** 136
[36] Ahn K, Yoo D S, Prasad D H, Lee H-W, Chung Y-C and Lee J-H 2012 *Chem. Mater.* **24** 4261
[37] Dohcevic-Mitrovic Z, Radovic M, Scepanovic M, Grujic-Brojcin M, Popovic Z, Matovic B *et al* 2007 *Appl. Phys. Lett.* **91** 203118
[38] Jais A A, Ali S M, Anwar M, Somalu M R, Muchtar A, Isahak W N R W *et al* 2017 *Ceram. Int.* **43** 8119
[39] Ali S M, Anwar M, Abdalla A M, Somalu M R and Muchtar A 2017 *Ceram. Int.* **43** 1265
[40] Matović B, Stojmenović M, Pantić J, Varela A, Žunić M, Jiraborvornpongsa N *et al* 2014 *Asian Ceram. Soc.* **2** 117
[41] Xiaomin L, Qiuyue L, Lili Z and Xiaomei L 2015 *J. Rare Earths* **33** 411
[42] Singh V, Babu S, Karakoti A S, Agarwal A and Seal S 2010 *J. Nanosci. Nanotech.* **10** 6495
[43] Wang F-Y, Wan B-Z and Cheng S 2005 *J. Solid State Electrochem.* **9** 168
[44] Chockalingam R G K and Basu S 2014 *J. Power Sources* **250** 80